Raman Optical Activity of a Purely σ-Bonded Helical Chromophore: (−)-(*M*)-σ-[4]Helicene

by **Werner Hug*** and **Gérard Zuber**

Institut de Chimie Physique, Université de Fribourg, Pérolles, CH-1700 Fribourg

and **Armin de Meijere** and **Alexander F. Khlebnikov**

Institut für Organische Chemie der Universität Göttingen, Tammannstrasse 2, D-37077 Göttingen

and **Hans-Jürgen Hansen**

Organisch-chemisches Institut der Universität Zürich, Winterthurerstrasse 190, CH-8057 Zürich

The recent synthesis of enantiomerically pure (−)-(*M*)-σ-[4]helicene has provided an archetype helical model system for vibrational optical activity, comparable to what π-helicenes represent in the field of electronic optical activity. We present the first measurements and the first calculations of the *Raman* optical activity (ROA) of this interesting molecule. Observed and calculated ROA is large throughout the vibrational spectrum, in agreement with expectations, and spectacular effects, with Δ values close to 0.5%, occur in the 900-cm^{-1} region. Agreement between the experimental spectrum and the theoretical one, calculated with density-functional theory for the vibrational part and *Hartree-Fock* linear response theory for the molecular electronic tensors, is excellent, clearly the best that has been achieved to date in the field. This allows us to place confidence in the results of an analysis of *Raman* and ROA scattering generation in the molecule, obtained by a newly developed graphical procedure for extracting this kind of information from *ab initio* calculations. One finds that relative contributions made by carbon and hydrogen atoms can be comparable in size, but can also vary considerably, even between closely lying vibrations, and that, for most vibrations, the generation of ROA difference intensity is distributed rather differently than that of *Raman* intensity over the shape of the molecule. The sign of the ROA is, for the set of vibrations in the 900-cm^{-1} region, which we analyze in detail, determined by coupling terms between the two halves of the molecule, while *Raman* intensity is primarily generated within the two fragments, with coupling terms between them only adding to or substracting from it.

Introduction. – The molecules chosen as model systems in the first successful observations of *Raman* optical activity (ROA) and vibrational circular dichroism (VCD) of molecular origin owed their chirality to the presence of a stereogenic C-atom carrying four different substituents [1][2]. The rigid frame of bicyclic terpenes was soon included in the list of model chromophores in vibrational optical activity [3][4]. Both systems also served as vehicles for the first successful recording of entire vibrational optical-activity spectra [5]. It subsequently became clear that the three-dimensional rigid structure of bicyclic compounds not only provided the benefit of the absence of conformational mobility, but also tended to yield sizable chiroptical effects throughout the vibrational spectrum. Bicyclic terpenes, α-pinene in particular, have become standard compounds for calibrating ROA and VCD spectrometers, and for comparing their performance [6][7].

A plethora of other kinds of molecules, considered suitable as model compounds for vibrational optical activity for one reason or another, has since been investigated.

The choice was often driven by the desire to be able to rationalize observed data with the help of simplifying theoretical model calculations. Ingenious and aesthetically pleasing as they might be, simplifying models have, however, largely failed to account for the vibrational optical activity of inherently chiral chromophores, as well as of molecules such as the above-mentioned bicyclic terpenes. Up to the advent of the direct, or *ab initio*, calculation of vibrational optical activity [8][9] much of the interpretative work on ROA and VCD spectra has, therefore, been limited to molecules with a few clearly distinguishable interacting groups, and to a few prominent, well-understood vibrational bands.

Within a short span of time, the *ab initio* calculation of vibrational optical activity proved more successful than the *ab initio* calculation of the optical activity of molecular electronic transitions [10]. This can be traced to the fact that the harmonic approximation is generally sufficient for the vibrational part, that the calculation of normal modes in this approximation is easy in comparison to the calculation of excited electronic states, and that electronic chiralty, as has been shown explicitly for ROA [11], makes only a minor contribution to vibrational optical activity.

Although the inherently helical hydrocarbon [4]triangulane had first been prepared in 1973 [12], it was then only available in its racemic form. The molecule, which may also be designated σ-[4]helicene, can be considered to represent the archetype helical chromophore in ROA and VCD in the same way that [6]helicene does in electronic optical activity. It may likewise be seen as the first member of a series of analogous molecules with an increasing number of spirocyclopropane groups. In spite of inherent helicity no longer presenting the obstacle to the computation of ROA and VCD that it did a decade ago, no theoretical work on this unique vibrational model chromophore has so far been published. The recent synthesis of enantiomerically pure $(-)$-(M)-σ-[4]helicene [13] has provided the incentive for a theoretical study of the molecule. Moreover, a newly developed *Raman* optical-activity spectrometer [14] made it possible to measure the vibrational optical activity with a far higher precision than before achieved. This gives a unique occasion for a detailed comparison of the theoretical and experimental data on this helical model system.

Measured Spectra. – There are three circular-polarization schemes and three preferred geometrical configurations that can be used to measure *Raman* optical-activity spectra. Each set-up has specific advantages and disadvantages [7][11]. The present measurements were done in a scattered circular-polarized (SCP) backscattering (scattering angle π) configuration on an instrument (*Fig. 1*) developed to exploit the benefits of this particular arrangement [14]. The sample is irradiated with time-average depolarized light, and the number of right, $N_R(\pi,\Delta\tilde{\nu})$, and left, $N_L(\pi,\Delta\tilde{\nu})$, circularly polarized scattered photons is separately but simultaneously recorded on the two halves of a charge-coupled device for all wavelengths of interest. The sum $N_R(\pi,\Delta\tilde{\nu}) + N_L(\pi,\Delta\tilde{\nu})$, as a function of the wavenumber shift $\Delta\tilde{\nu}$, yields the *Raman* and the difference $N_R(\pi,\Delta\tilde{\nu}) - N_L(\pi,\Delta\tilde{\nu})$ the ROA spectrum. There is no modulation required between right and left circular-polarization states, and the influence of dust and thermal schlieren in the sample, as well as of intensity fluctuations in the laser, is, therefore, greatly diminished. Small differences in the transmission characteristics of the two optical branches of the instrument are compensated by periodically interchanging their

function through the switching of the liquid crystal retarder shown in *Fig. 1* (for more details on the optics and the data acquisition logics, *cf.* [14]).

The illumination time of the sample, which excludes detector read-out overhead, was 3/4 h. The probe size was only 35 µl, a value made possible by the use of a newly developed cylindrical backscattering cell to be described elsewhere [15]. Laser power at the sample was kept at 115 mW, though ten times this value can be used in the instrument. The low value was chosen as a precautionary measure, in view of the uniqueness of the volatile sample, and in view of the highly strained structure of the molecule. The precaution would probably not have been necessary, as the probe proved to be stable and devoid of fluorescent impurities, as well as of light absorbing dust. The relatively long recording time, together with the extremely high optical throughput of the instrument, yielded a ROA spectrum of exceptional quality despite the low laser power (*Fig. 2*).
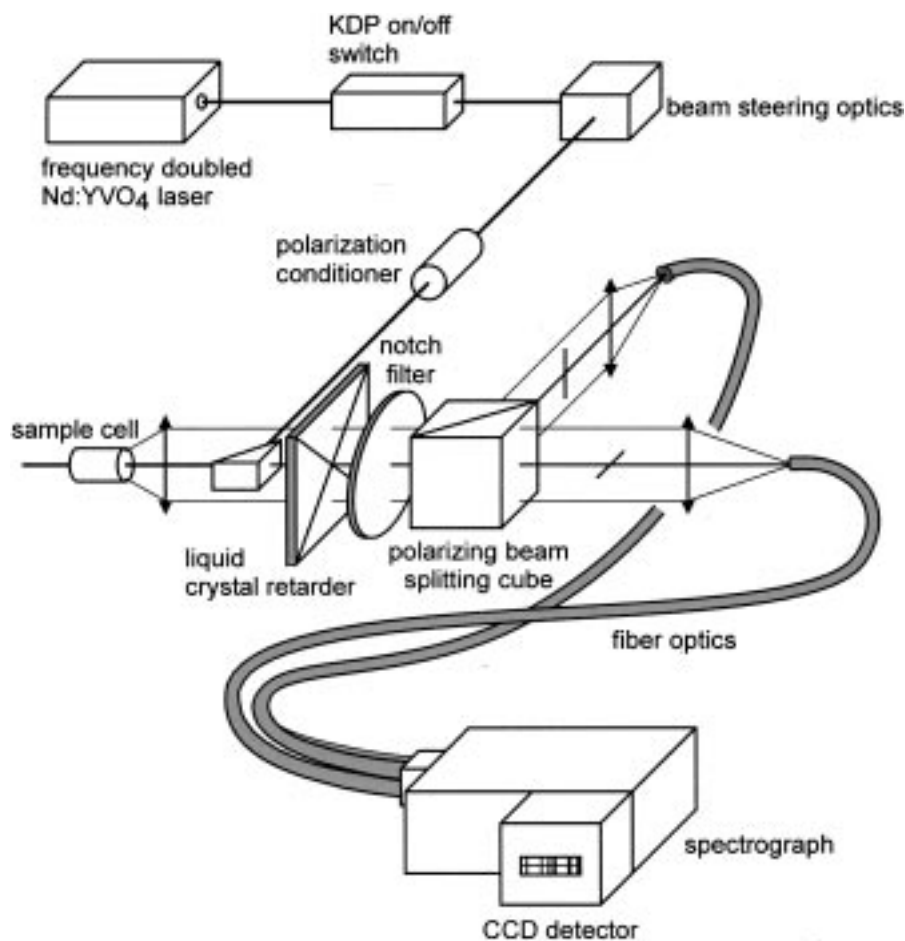

Fig. 1. *Simplified optical layout of the backscattering SCP instrument used for recording the experimental spectra.* The backscattering light is circular-polarization-analyzed, with the intensities of the right and left components being simultaneously measured for the spectral range of interest.
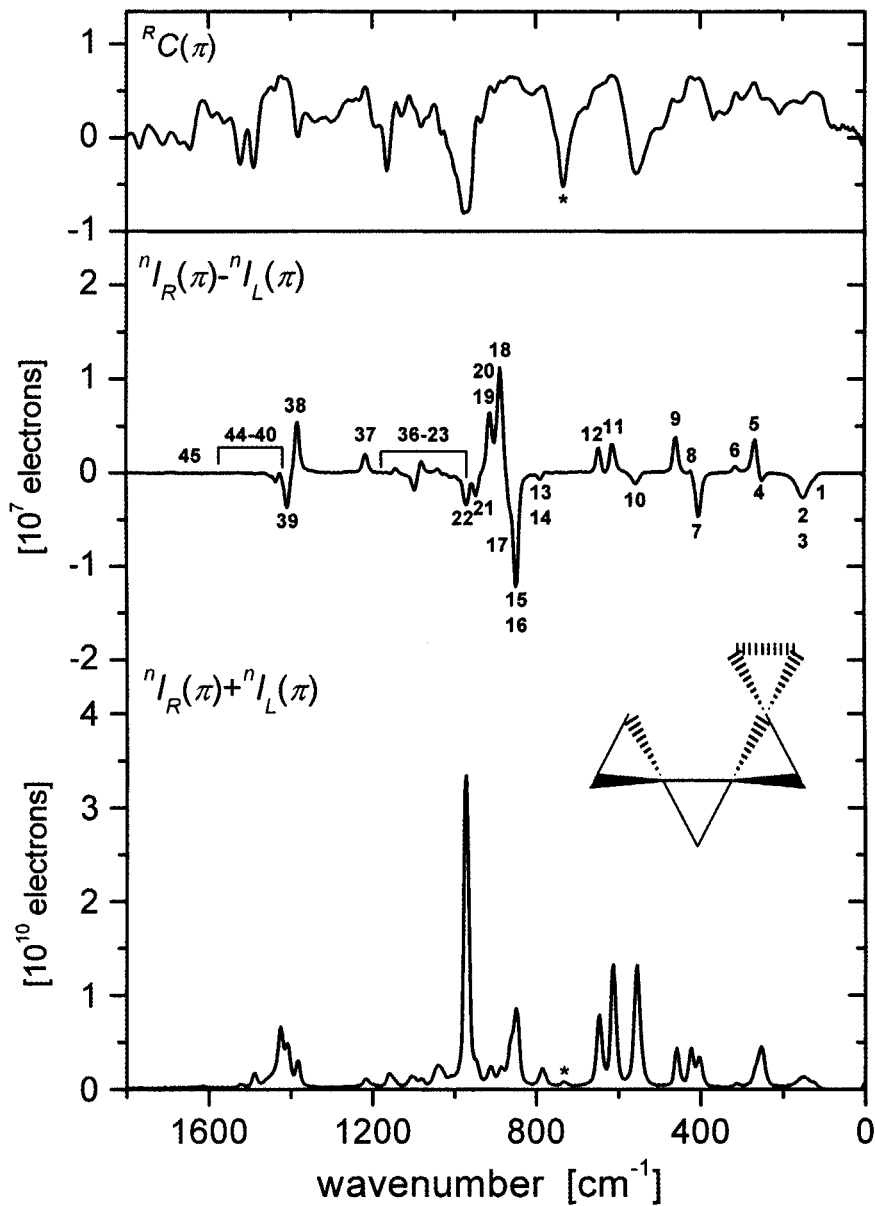
Fig. 2. *Experimental spectra of (−)-σ-(M)[4]helicene. Top curve:* degree of circularity $^{R}C(\pi)$. *Middle curve:* backscattering SCP circular-difference spectrum. *Bottom curve:* circular-sum spectrum. Onset of cut-off by the holographic notch-filter is at *ca.* 100 cm^{-1}. Sample size 35 μl, excitation wavelength 532 nm, average resolution 7 cm^{-1}, laser power at sample 115 mW, sample illumination time 42 min, total excitation energy 290 J. Indicated charge is the charge per CCD column (2.4 cm^{-1} spectral width). The band marked with a star is due to an impurity (see text).

As expected, the observed vibrational optical activity of the helical chromophore proved large. To bring the size of some of the observed Δ values to the fore, the ratio

$$\Delta(\pi, \Delta\tilde{\nu}) = \frac{{}^nI_R(\pi, \Delta\tilde{\nu}) - {}^nI_L(\pi, \Delta\tilde{\nu})}{{}^nI_R(\pi, \Delta\tilde{\nu}) + {}^nI_L(\pi, \Delta\tilde{\nu})} \tag{1}$$

is shown in *Fig. 3*, together with the theoretical one (the calculation of which will be explained in the following section). We stress that the curve represents the ratio obtained by the direct division of measured values, throughout the observed wave-number range, with no correction for base-line shifts, and with minimal smoothing only by the third-order five-point *Savitzky-Golay* procedure. It is seen that sizable Δ values are found for skeletal and CH-bending modes, but that the largest ones, reaching close to 0.5%, occur in the 900-cm^{-1} region. To our knowledge, this represents the largest Δ value observed in SCP and ICP backscattering for excitation light with a wavelength of the order of 500 nm, at any rate for a molecule other than large helical proteins (where background problems, signal-to-noise ratios, and overlapping vibrational bands render the assignment of precise Δ values in general meaningless).

The uppermost curve in *Fig. 2* represents the degree of circularity C of the scattered radiation for right circular incident light, measured in backscattering. It is given by

$$^RC(\pi) = \frac{{}^RI_R(\pi) - {}^RI_L(\pi)}{{}^RI_R(\pi) + {}^RI_L(\pi)} \tag{2}$$

In the far-from-resonance limit, which applies here, C characterizes the relative size of the anisotropic and isotropic parts of the electric dipole-dipole scattering tensor[1]. The better known depolarization ratio $\rho_\perp$ is related to $^RC(\pi)$ by

$$\rho_\perp = \frac{1 + {}^RC(\pi)}{3 - {}^RC(\pi)} \tag{3}$$

The depolarized *Raman* spectrum can, therefore, be obtained from the polarized one shown in *Fig. 2* with the help of C. To qualitatively judge the polarization of the various *Raman* bands, it suffices to remember that one has

$$\rho_\perp = 3/4 \text{ for } {}^RC(\pi) = 5/7 \qquad \text{(fully depolarized band)}$$

$$\rho_\perp = 1/3 \text{ for } {}^RC(\pi) = 0$$

$$\rho_\perp = 0 \text{ for } {}^RC(\pi) = -1 \qquad \text{(fully polarized band)}$$

Thus, the intense band at 971 cm^{-1} (vibrational mode 22) is fairly polarized ($^RC(\pi) = -0.89$, $\rho_\perp = 0.028$), but all other bands show values for $^RC(\pi)$ more positive than -0.39 ($\rho_\perp > 0.18$), with the exception of a band at 732 cm^{-1} ($^RC(\pi) = -0.51$, $\rho_\perp = 0.14$).

---

[1]   For this statement to be precise in the case of optically active compounds, ^RI_R in *Eqn. 2* needs to be replaced by the average value of ^RI_R and ^LI_L. In practical terms, the difference is negligible, but it is measurable. It corresponds to DCP$_I$ ROA.
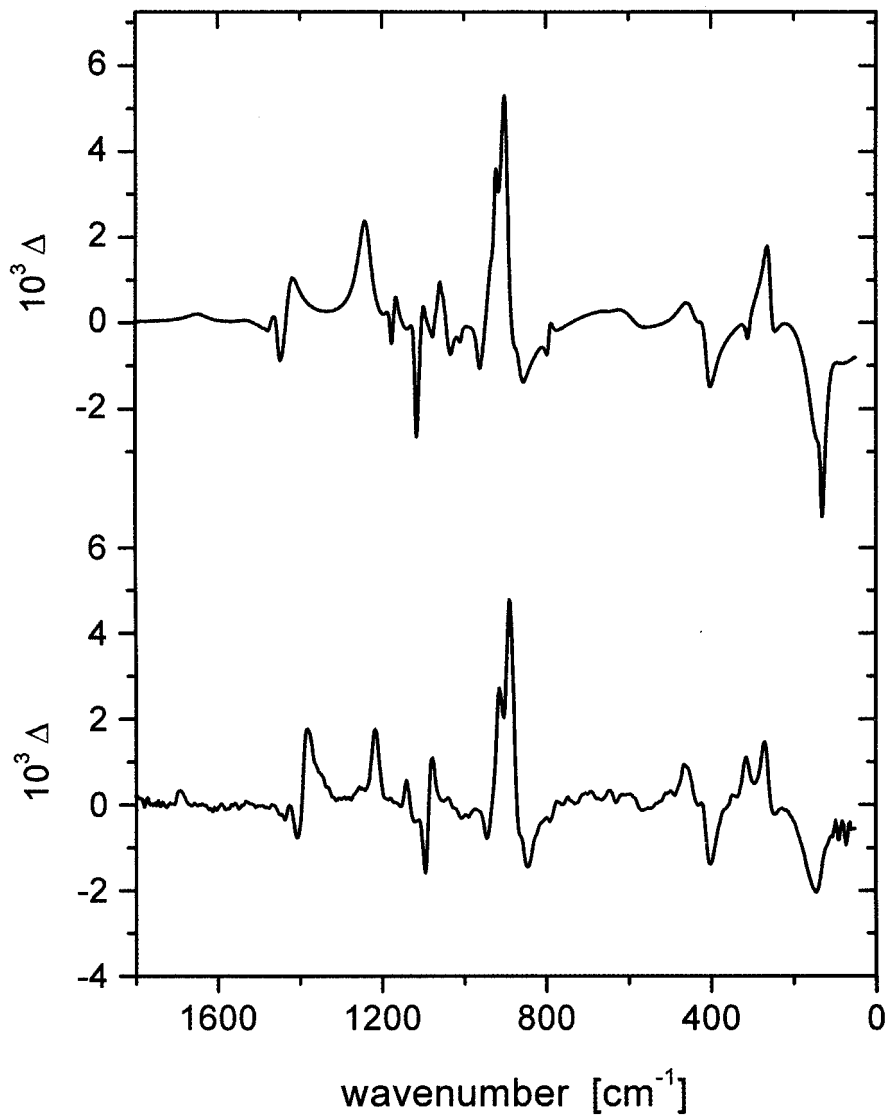
Fig. 3. *Calculated* (top) *and measured* (bottom) $\Delta(\Delta\tilde{\nu})$ *curve for SCP backscattering.* The experimental curve was obtained by the direct division, CCD column by CCD column, of the measured circular difference by the circular-sum intensity, with minimal smoothing only applied to the result (five points third-order *Savitzky-Golay*).

Our calculations safely rule out a fundamental vibrational transition at this wavenumber shift. The small *Raman* band at 732 cm^{-1}, which shows no ROA on the scale used in *Fig. 2*, must, therefore, either represent an overtone or a combination band, or it must be due to an impurity. An overtone or a combination band appearing with the observed intensity would have to borrow it from a close-lying fundamental. As

there is no polarized fundamental in the vicinity of the 732-cm^{-1} band, the *Raman* band must be due to an impurity[2]). This example shows the considerable analytical potential of the rarely measured degree of circularity.

Calculation of Scattering Cross Sections. – The differential scattering cross sections underlying the spectra of *Fig. 2* are given by the expressions [16]

$$^nd\sigma(\pi)_{SCP} = K(90a^2 + 14\beta^2)d\Omega \tag{4a}$$

$$-\Delta^nd\sigma(\pi)_{SCP} = 4(K/c)(12\beta_G^2 + 4\beta_A^2)d\Omega \tag{4b}$$

If σ is defined as the rate at which photons are removed from the incident beam by scattering, relative to the rate at which they cross a unit area perpendicular to the direction of propagation of the incident beam, then for σ in units of m^2 the constant K is given by [11]

$$K = K_p = \frac{1}{90}\left(\frac{\mu_0}{4\pi}\right)^2\omega_p^3\omega_0 = \frac{10^7}{9}\pi^2\mu_0^2c^4\tilde{v}_p^3\tilde{v}_0 \tag{5a}$$

$$\tilde{v}_p = \frac{\omega_p}{200\pi c} = \frac{\omega_0}{200\pi c} \pm \Delta\tilde{v}_p \tag{5b}$$

where $\omega_0 = 2\pi v_0$ is the frequency of the incident and ω_p the frequency of the scattered light, $\Delta\tilde{v}_p$ the *Raman* frequency shift (in cm^{-1}), c the speed of light (in ms^{-1}), and μ_0 the permeability of the vacuum; a^2 is the isotropic and β^2 the anisotropic invariant of the molecular electric dipole-dipole transition tensor, and aG' (which appears in *Eqn. 6b* below) and β_G^2 are the isotropic and anisotropic invariants, respectively, due to cross products of this tensor with the electric dipole-magnetic dipole transition tensor, and β_A^2 the anisotropic invariant due to its cross products with the electric dipole-electric quadrupole transition tensor.

Eqn. 4b is written with the sign convention right circular minus left circular, which is, unfortunately, used for presenting data in circular difference scattering. This leads to the minus sign in front of $\Delta\sigma = d\sigma_L - d\sigma_R$, which, as a molecular quantity, is defined in the standard optical-activity sign convention.

Eqns. 4a and *4b* are valid for an infinitely small light collection angle $d\Omega$. In a practical ROA experiment, a finite angle $\Delta\Omega$ must be used. In principle, in a comparison of theoretical and experimental results, integration of the theoretical expressions over the collection angle should be performed, with explicit consideration of the angular dependence of the scattering cross sections on the various invariants. For the current precision of calculated data and for the light-collection angle, which we employ [14], this degree of sophistication is not required. Quantitative comparison is, therefore, done on the basis of *Eqns. 4a* and *4b*.

Integration of angular dependence over the full solid angle of 4π is of interest, on the other hand, because it yields the molecular quantities σ and $\Delta\sigma$. They represent invariant combinations that do not depend, in the far-from-resonance limit, on a particular scattering geometry or on a particular circular-polarization scheme. One obtains [11]

---

[2])   *Note added in proof*: This analysis was confirmed by the measurement of a racemic sample for which the 732-cm^{-1} band was found to be absent.

$$^n\sigma_{SCP} = \frac{4\pi K}{3}(180a^2 + 40\beta^2) \qquad (6a)$$

$$-\Delta\,^n\sigma_{SCP} = \frac{8\pi K}{3c}(180aG' + 40\beta_G^2) \qquad (6b)$$

A remarkable aspect of *Eqn. 6b* is the absence of the quadrupole term β_A^2. It was shown, in the context of the first recording of polarized ROA spectra [17], that the quadrupole contribution can be separated from the magnetic dipole contributions by the sole use of polarized and depolarized right-angle scattering data. The resulting linear combination of aG' and β_G^2 corresponds to that appearing in *Eqn. 6b* and is, therefore, readily experimentally accessible.

Our new ROA instrument, while currently limited to backscattering, has been designed so that it will eventually also permit the simultaneous measurement of polarized and depolarized right-angle scattering. In view of the general nature of *Eqns. 6a* and *6b*, and in view of the fact that the combination of invariants represented by them will become routinely available in the future, *Eqns. 6a* and *6b* are used in the following, in lieu of *Eqns. 4a* and *4b*, for pictorial representations of distributed *Raman* and ROA scattering cross sections. The comparison of such pictures with backscattering spectra presents no difficulty for bands which are dominated by β^2 and β_G^2.

The molecular invariants appearing in *Eqns. 4a* to *6b* can, according the *Placzek* polarizability theory approach [18], be written as a sum of invariant mono- and dinuclear terms [19]. For the anisotropic invariant β_G^2, *e.g.*, one obtains

$$\beta_G^2 = \frac{\hbar}{400\pi c\Delta\tilde{\nu}}\sum_{\alpha,\beta} \boldsymbol{L}_{\alpha,p}^x \cdot \boldsymbol{V}(\beta_G^2)_{\alpha\beta} \cdot \boldsymbol{L}_{\beta,p}^x \qquad (7)$$

$\boldsymbol{L}_{\alpha,p}^x$ represents the *Cartesian* displacement vector of nucleus α of mass m_α in normal mode p, normalized so that $\sum_{\alpha,i} m_\alpha(L_{\alpha i,p}^x)^2 = 1$, and $\boldsymbol{V}(\beta_G^2)_{\alpha\beta}$ is a dyadic with the elements

$$V(\beta_G^2)_{\alpha i,\beta j} = \frac{1}{2}\sum_{\mu,\nu}\left[3\left(\frac{\partial\alpha_{\mu\nu}^e}{\partial x_i^\alpha}\right)_0\left(\frac{\partial G_{\mu\nu}'^e}{\partial x_j^\beta}\right)_0 - \left(\frac{\partial\alpha_{\mu\mu}^e}{\partial x_i^\alpha}\right)_0\left(\frac{\partial G_{\nu\nu}'^e}{\partial x_j^\beta}\right)_0\right] \qquad (8)$$

where $\alpha_{\mu\nu}^e$ and $G_{\mu\nu}'^e$ are *Cartesian* components of the purely electronic electric dipole-electric dipole and the imaginary part of the electric dipole-magnetic dipole polarizability tensor, respectively. Similar expressions hold for other invariants.

The displacement vectors $\boldsymbol{L}_{\alpha,p}^x$ in *Eqn. 7* were calculated with B3LYP density-functional theory and a 6-311G** basis set (*GAUSSIAN98* [20]). The calculation of the gradients of the electronic tensors of *Eqn. 8* was done with *Hartree-Fock* linear-response theory and *London* orbitals, as implemented in *DALTON* [21], at the B3LYP geometry. The basis set employed was specifically developed for the *Raman* and ROA calculation of polyatomic molecules (for technical details, *cf.* [22]). The aspect that we point out here is that the approach of the separate calculation of the vibrational and the electronic part, as done in the present work, leads to substantial additional freedom in the choice of the basis sets. Diffuse functions, *e.g.*, are of limited interest in the calculation of the displacement vectors $\boldsymbol{L}_{\alpha,p}^x$, but they are mandatory for the reliable computation of the tensor gradients in *Eqn. 8*. Conversely, it can be shown that many of the so-called polarization functions matter little in the calculation of tensor gradients,

though they are clearly important for $\boldsymbol{L}^x_{\alpha,p}$. Our new purpose-oriented basis sets for the calculation of tensor gradients, while based on the well-known aug-cc-pVDZ set, take advantage of this insight. They provide Δ values of a precision comparable to what can be achieved with aug-cc-pVDZ, but at a fraction of the cost.

Theoretical Spectra. – In keeping with what has become standard practice for presenting such data in vibrational optical activity [10], the calculated spectra in *Fig. 4* are shown in the form of band spectra. The height of the *Lorentzians* used to generate them corresponds to the calculated values of the scattering cross sections. Calculated numerical values are collected in *Table 1*. The loss of information, which is incurred by the conversion of line to band spectra, is balanced by the ease with which an overall comparison of calculated and measured data can be made, particularly in regions where vibrational bands overlap. For the σ-[4]helicene the principal problem area of this kind extends from 1000 cm^{-1} to 1200 cm^{-1} in the theoretical, and from 980 cm^{-1} to 1180 cm^{-1} in the experimental spectrum, and comprises vibrations 23 to 36. The finding that all of these vibrations are lumped together, as are vibrations 40 to 44 in the 1450-cm^{-1} to 1550-cm^{-1} region should, however, not be construed to mean that none of the experimental bands could, at least tentatively, be assigned. A more detailed discussion of both areas, based on additional data, is planned in later work.

The spectra shown in *Figs. 2 – 4* can be divided into three spectral regions reflecting the nature and composition of the vibrational modes. The first one extends from 50 to 750 cm^{-1} and comprises the modes 1 to 12. In these modes, the H-atoms move as if they were rigidly attached to the main atom frame, or more precisely, the particular fragment of the frame closest to them. The motion of these fragments often exerts a lever-like action on the H-atoms, so that their *Cartesian* displacement vectors do not need to be the same as those of the C-atoms that carry them. CH-Bond stretching and bending is negligible, however. This picture follows from the graphical inspection of normal modes. It can be rationalized by a breakdown of the total number of vibrations, based on a separation of C,C and C,H internal coordinates. When the 6 CH$_2$ groups are treated as pseudo-atoms, one will have $3 \times 9 - 6 = 21$ vibrational modes for the molecule. Of these, 12 will be combinations of ring-stretching and ring-breathing modes, 3 of them leading to large-scale skeletal deformation, which form part of region one, and 9 of high enough frequency to invalidate the pseudo-atom assumption. One is, therefore, left with the $21 - 9 = 12$ vibrations actually observed in region 1.

The next region, covering vibrations 13 through 37, extends from 750 cm^{-1} to 1300 cm^{-1}, with a clearly different aspect of its vibrational modes. Here, the H-atoms tend to move against the C-atom frame, in most vibrations in a combination of rocking, twisting, and wagging motions. The mix-up of these internal coordinates accounts for 18 of the 25 vibrations calculated for region 2. The 7 additional ones can easily be explained by the mixing-in of the displacement coordinates of ring stretching and breathing motions. This leaves 2 sets of C coordinates to contribute to vibrations of higher frequency.

The third region covers the range from 1300 to 1700 cm^{-1} and comprises the 8 vibrational modes 38 to 45. Vibrations 38 through 44 are dominated by H-scissoring motions. The presence of 7, rather than the expected 6 vibrations of this kind shows that C-atom motion is not negligible. Most of it occurs in the two vibrations 38 and 44 of
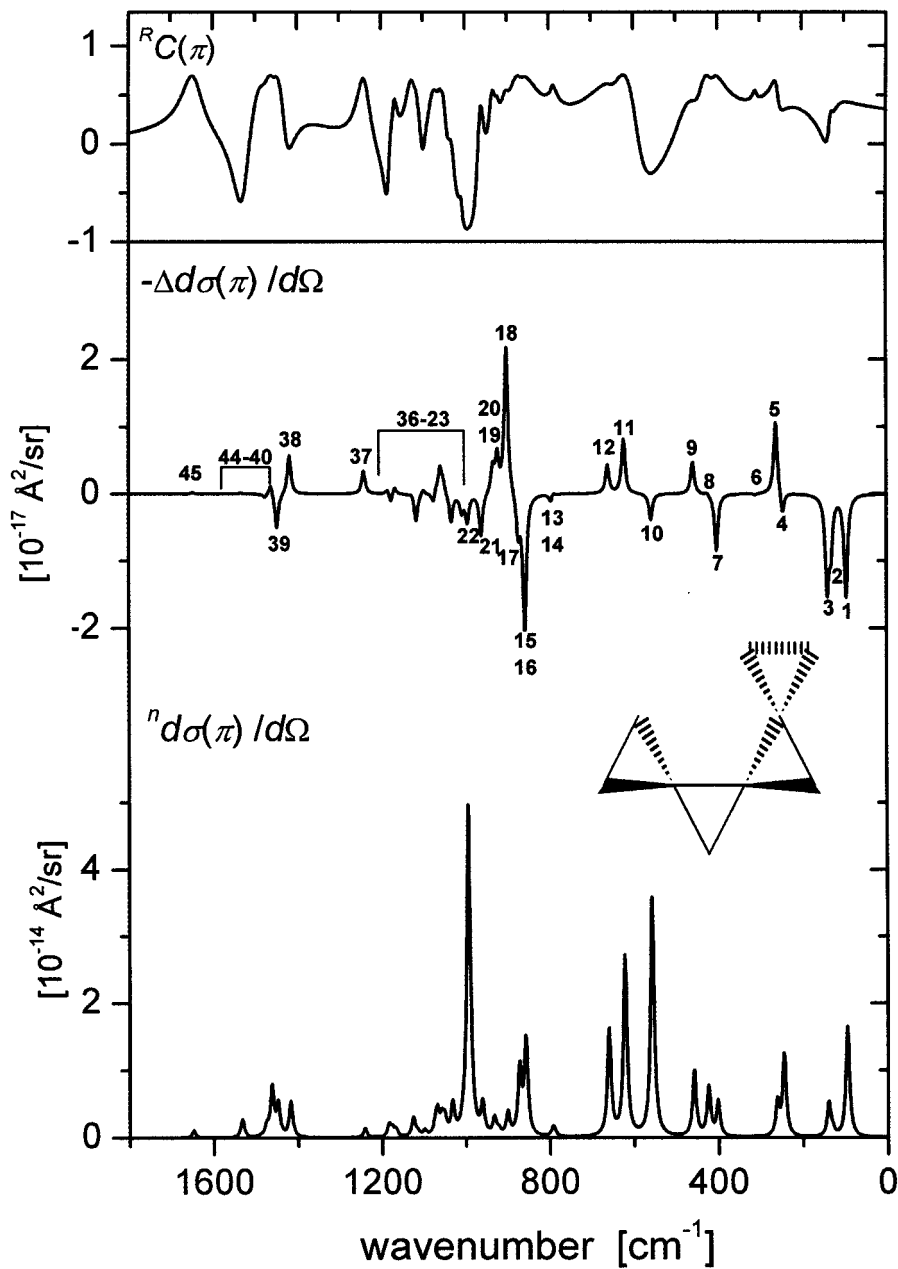
Fig. 4. *Calculated spectra of (−)-(M)-σ-[4]helicene. Top curve:* degree of circularity $^RC(\pi)$. *Middle curve:* backscattering SCP circular-difference spectrum. *Bottom curve:* circular-sum spectrum. Normal coordinates: B3LYP density-functional theory with 6-311G** basis set. Gradients of electronic tensors: SCF linear-response theory with a basis set derived from aug-cc-pVDZ (see text and [22]). Full width at half-maximum height of the *Lorentzians* used to represent vibrational bands is 10 cm^{-1}, with peak-height corresponding to the calculated differential circular sum and difference-scattering cross sections. Temperature assumed for the population of vibrational states: 25°. Frequencies are unscaled.

Table 1. *Calculated* Raman *and ROA SCP Backscattering Data of the 57 Fundamentals of (−)-(M)-σ-[4]Helicene.* Also indicated is the degree of circularity $^RC(\pi)$. Computational parameters as for *Fig. 4*. Horizontal lines separate the 4 spectral regions discussed in the text.

Mode	$\Delta\tilde{\nu}$ [cm^{-1}]	$^nd\sigma(\pi)_{SCP}$ [10^{-14} Å^2/sr]	$-\Delta^nd\sigma(\pi)_{SCP}$ 10^{-17} Å^2/sr]	$10^3\,\Delta(\pi)_{SCP}$	$^RC(\pi)$
1 (A)	96	1.619	− 1.497	− 0.92	0.431
2 (B)	132	0.081	− 0.720	− 8.89	0.714
3 (A)	141	0.491	− 1.330	− 2.71	− 0.024
4 (A)	246	1.202	− 0.345	− 0.29	0.337
5 (B)	262	0.490	1.085	2.21	0.714
6 (B)	310	0.012	− 0.017	− 1.38	0.714
7 (A)	402	0.509	− 0.846	− 1.66	0.708
8 (B)	424	0.726	0.040	0.06	0.714
9 (A)	458	0.972	0.477	0.49	0.441
10 (A)	557	3.575	− 0.391	− 0.11	− 0.309
11 (B)	622	2.669	0.808	0.30	0.714
12 (A)	660	1.575	0.427	0.27	0.617
13 (B)	791	0.098	0.074	0.75	0.714
14 (A)	795	0.082	− 0.143	− 1.74	0.463
15 (B)	857	0.411	− 0.864	− 2.11	0.714
16 (A)	858	1.026	− 1.209	− 1.18	0.685
17 (B)	873	0.973	− 0.579	− 0.59	0.714
18 (A)	901	0.330	2.195	6.64	0.582
19 (B)	922	0.074	0.534	7.24	0.714
20 (B)	933	0.248	0.363	1.47	0.714
21 (A)	961	0.446	− 0.636	− 1.43	0.693
22 (A)	994	4.922	− 0.408	− 0.08	− 0.883
23 (B)	1007	0.116	− 0.257	− 2.22	0.714
24 (A)	1032	0.442	− 0.426	− 0.96	0.145
25 (B)	1052	0.229	0.168	0.73	0.714
26 (B)	1058	0.227	0.377	1.66	0.714
27 (A)	1069	0.309	0.094	0.30	0.601
28 (B)	1073	0.045	0.034	0.77	0.714
29 (A)	1074	0.117	− 0.205	− 1.75	0.661
30 (A)	1099	0.083	0.083	1.00	− 0.286
31 (B)	1116	0.066	− 0.410	− 6.21	0.714
32 (A)	1126	0.277	0.042	0.15	0.709
33 (B)	1167	0.094	0.119	1.27	0.714
34 (A)	1175	0.104	− 0.225	− 2.16	0.297
35 (B)	1175	0.009	0.075	8.65	0.714
36 (A)	1184	0.180	0.078	0.43	− 0.729
37 (B)	1241	0.135	0.341	2.53	0.714
38 (A)	1418	0.523	0.587	1.12	− 0.075
39 (B)	1448	0.470	− 0.533	− 1.13	0.714
40 (B)	1462	0.115	0.162	1.40	0.714
41 (A)	1463	0.611	0.016	0.03	0.712
42 (A)	1476	0.150	− 0.054	− 0.36	0.596
43 (B)	1489	0.011	− 0.004	− 0.36	0.714
44 (A)	1533	0.271	0.016	0.06	− 0.624
45 (B)	1648	0.110	0.023	0.21	0.714
46 (B)	3090	0.336	− 0.846	− 2.52	0.714
47 (A)	3090	4.166	0.864	0.21	− 0.852
48 (B)	3105	0.348	− 0.513	− 1.47	0.714
49 (A)	3106	2.089	0.577	0.28	− 0.193

Table 1 (cont.)

Mode	$\Delta\tilde{\nu}$ [cm^{-1}]	$^{n}d\sigma(\pi)_{SCP}$ [10^{-14} Å^2/sr]	$-\Delta^{n}d\sigma(\pi)_{SCP}$ 10^{-17} Å^2/sr]	$10^3\,\Delta(\pi)_{SCP}$	$^{R}C(\pi)$
50 (B)	3109	0.003	− 0.018	− 5.49	0.714
51 (A)	3110	6.649	− 0.007	− 0.00	− 0.932
52 (A)	3171	1.949	0.150	0.08	0.698
53 (B)	3172	0.404	− 0.519	− 1.28	0.714
54 (B)	3181	0.846	1.695	2.00	0.714
55 (A)	3182	1.574	− 1.292	− 0.82	0.711
56 (B)	3195	0.450	0.466	1.04	0.714
57 (A)	3196	1.443	− 0.688	− 0.48	0.648

species A and is confined to the two outer spiro-C-atoms C(3) and C(7) (for the numbering, see *Fig. 5*). The additional vibration 45 of species B, which brackets region 3 at the upper end, is, similarly to vibration 37, which brackets region 2, dominated by the motion of the central spiro-C-atom C(5). In vibration 45, the combined result of the displacement of all three spiro-C-atoms C(5), C(3), and C(7) is a breathing motion, out-of-phase for the two inner cyclopropane rings. The motion of the H-atoms is, as one would expect, of the scissoring kind, but small in comparison to that of the 3 spiro C-atoms.
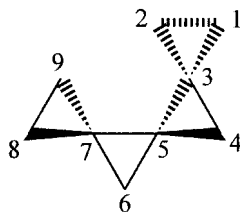
Fig. 5. *Structure of numbering of (M)-trispiro[2.1.1.2]nonane (=(−)-(M)-σ-[4]helicene)*

The CH-stretching region, which is not shown here, represents a fourth spectral region extending from 3050 to 3200 cm^{-1}. The symmetric stretching vibrations 46 to 51 are found in the 3050 to 3125 cm^{-1} range, and the antisymmetric ones 52 to 57 in the 3125 to 3200 cm^{-1} range. All stretching vibrations occur in neat pairs of close to degenerate modes of species A and B.

Most of the attention in the following section will be devoted to the salient features of region 2. With respect to the size of observed ROA, it is clearly the most interesting one. Rather unfortunately, it is also, by far the most difficult, to analyze. The problems encountered in the characterization of its vibrational modes can be appreciated from a comparative inspection of the pair of vibrations 13 and 14 (species B and A, resp.) occurring at the lower end of the range, with the pair 34 and 35 (species A and B, resp.), which is found close to the upper end. The *Cartesian* displacement vectors are shown in *Fig. 6* with an explanation of the details of the graphical representation given in the following section. One sees that the motion of the H-atoms, though not identical for the two pairs, is quite similar, essentially a twisting motion, with a more substantial rocking content for the pair (13, 14) at lower frequency.
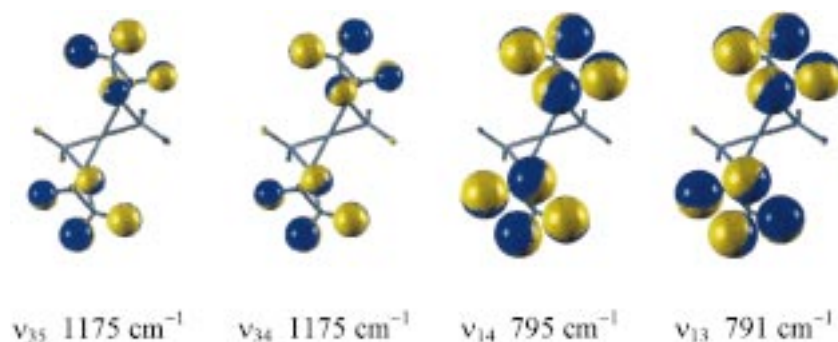
ν_{35} 1175 cm^{-1} ν_{34} 1175 cm^{-1} ν_{14} 795 cm^{-1} ν_{13} 791 cm^{-1}

Fig. 6. *Graphical representation of pairs of the A, B species-related vibrations ν_{13}, ν_{14}, and ν_{34}, ν_{35}.* The smaller size of the H excursions in the higher-frequency pair is a consequence of the larger contribution by C-atoms, and of the presence of the factor $1/\sqrt{\Delta\tilde{\nu}}$. For details, see the section on pictorial representations.

Most of the distinction between the two pairs of vibrations comes about by the H-atoms of the two CH_2 groups of the outer rings moving out-of-phase in the lower-frequency pair, and in-phase in the higher-frequency pair. The angular momentum generated by the in-phase movement, in turn, is locally compensated by the counter-movement of the C-atoms of the CH_2 groups, which explains the substantially larger contribution of the C-atom motion in the higher-frequency pair. Altogether, the change in phase and the ensuing change in composition entail a calculated change in energy of almost 380 cm^{-1}, a value larger than the wavenumber difference for wagging, twisting, and rocking motions. It is thus quite understandable that the distinction between these group frequencies is largely blurred throughout region 2.

The mix-up of vibrational group and skeletal modes in region 2 can only be computationally handled if the *ab initio* procedure and the basis set used yield the correct relative size for H,C and C,C force constants. Absolute values of calculated vibrational frequencies are far less critical than relative values, a conclusion reached already in the different context of the calculation of the mixing of Me- and Ph-group vibrations [23]. For hydrocarbons, at least, the combination B3LYP and 6-311G** seems to work well in this respect, better than other combinations we have tested, including ones with MP2 and cc-pVDZ [22]. This is borne out by the quality of the data shown in *Figs. 3* and *4*. The separation of molecular vibrations into a class of species A, and one of species B, which do not mix, helps of course, but the agreement between computed and measured spectra, in particular for the rather-difficult-to-calculate Δ values shown in *Fig. 3*, is nevertheless astounding.

A detailed comparison, vibration by vibration, is not possible in the 1000-cm^{-1} to 1200-cm^{-1} range where extensive cancellation of large positive and negative ROA occurs. One must be aware here that small variations in the shape of bands, for which a uniform value is assumed in the computed Δ spectrum, and of the value of the calculated center frequency can cause massive changes in appearance, an aspect which should also be kept in mind when judging the 300-cm^{-1} area. In contrast, the negative-positive-negative feature exhibited by the experimental Δ spectrum in the 900-cm^{-1} area is closely matched by the calculated one.

Pictorial Interpretation. – The dominant central negative-positive feature of the ROA spectrum of (−)-(*M*)-σ-[4]helicene is shown in *Fig. 7* on an expanded scale. There are 6 vibrations that contribute to it. The negative and the positive part are each made up by one vibration of species A and two of species B, with modes of species A showing larger ROA than those of species B. Vibration 18 in particular, calculated at 901 cm^{-1}, has with $-\Delta^n d\sigma(\pi)_{SCP} = 2.19 \times 10^{-17}$ Å^2/sr the largest calculated circular difference differential-scattering cross section of all 57 fundamentals of the molecule. It yields the dominant positive peak at 887 cm^{-1} in the experimental spectrum, with the two vibrations 19 and 20 of species B being jointly responsible for the second largest positive peak at 912 cm^{-1}. In contrast, the largest negative peak in the experimental spectrum comes about by the superposition of the negative envelopes of two vibrations, mode 15 of species B, and 16 of species A, both calculated at almost the same wavenumber shift of *ca.* 858 cm^{-1}. The fact that, in the experimental spectrum, the size of the largest negative
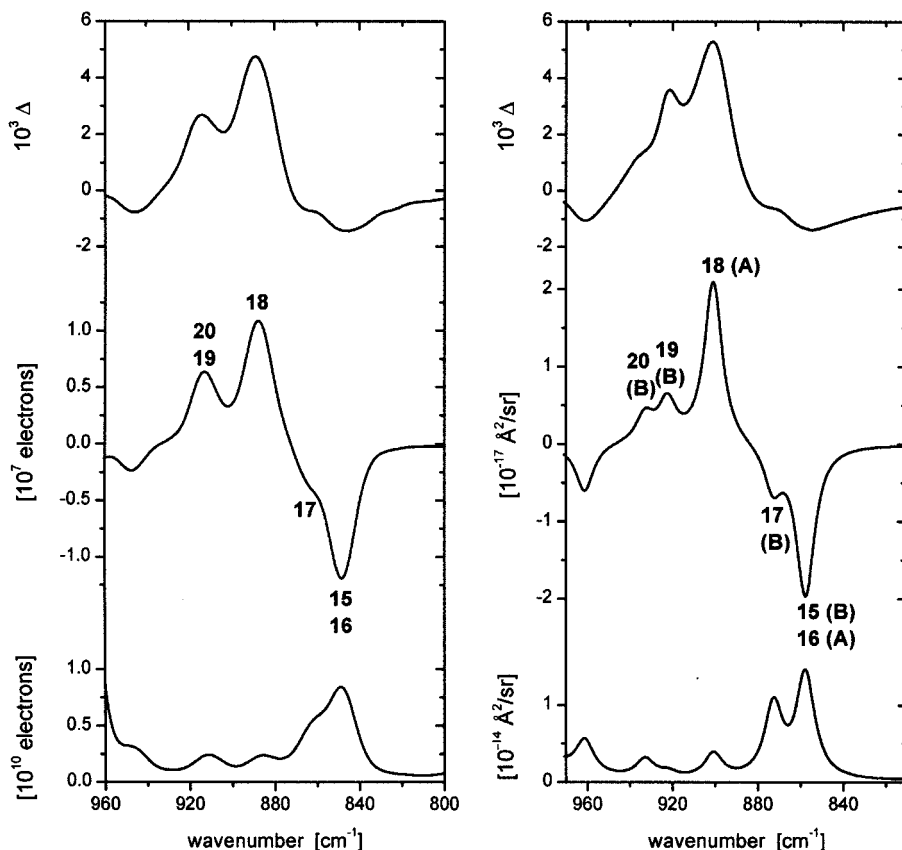

Fig. 7. *Central negative-positive feature of the ROA spectrum of (−)-(*M*)-σ-[4]helicene.* The measured data are shown on the left, and the calculated ones on the right side. *Top:* backscattering SCP *Δ* curve. *Middle:* circular difference spectrum. *Bottom:* circular-sum spectrum. Experimental conditions and computational parameters are as in *Figs. 2* and *4*.

band exceeds that of the largest positive one, while in the calculated spectrum the opposite is true, probably comes about by the envelope of vibration 17, seen as a shoulder only on the left side of the dominant negative peak in the experimental spectrum, contributing more to this peak than in the calculated spectrum.

How sure can we be that there are indeed two vibrations hidden under the observed negative peak at 849 cm^{-1}? We believe that this interpretation is on solid ground. First, there is the aspect of the almost quantitative agreement of the calculated and observed $\Delta(\pi)$ curves. Second, the two vibrations 15 and 16 are of different species. They do not mix or repel each other, and so can be degenerate without losing their identity. If, on the other hand, one of them occurred at a somewhat different wavenumber shift, then it could, almost for sure, be identified in either the sum, the difference, the $\Delta(\pi)$, or the $^R C(\pi)$ curve. Moreover, we have performed a number of additional calculations with different basis sets, including the MP2 method. They all yield a large, negative ROA for mode 16 of species A, and a negative ROA of variable size for mode 15 of species B. The ROA intensity lost by mode 15 appears shifted to mode 17 of the same species, and the energetic splitting between mode 15 and 17 is increased in most calculations. Despite these changes, modes 15 and 16 retain their identities, and their shapes, as characterized by the displacement vectors, remain similar to that of vibrations 15 and 16 as shown in *Fig. 8,a*. The fact that B3LYP density-functional theory best reproduces the near degeneracy of the two modes, as well as the position and intensity of vibration 17, has, as a matter of fact, been one of the criteria for our choice of the DFT results for the present discussion.

Also shown in *Fig. 8,a*, is this third negative vibration 17. The three positive modes 18, 19, and 20 are presented in *Fig. 8,b*. For most polyatomic chiral molecules, the use of arrows to represent displacement vectors leads to a hopelessly confusing picture, unless three-dimensional stereoscopic projections are used. We are, therefore, drawing spheres on atoms, centered at the equilibrium position of the nuclei [19]. The size of the spheres is chosen proportional to $|\boldsymbol{L}_{\alpha,p}^x|/\sqrt{\Delta\tilde{\nu}}$, and the direction of nuclear motion is indicated by coloring or shading. As can be seen from *Eqn. 7*, the surface of the spheres is proportional to the weight that nuclear motion has in polarizability theory expressions of molecular invariants and scattering cross sections. In judging the size of excursions, one must keep in mind the role atomic mass plays in the normalization of *Cartesian* displacement vectors. In normal modes where the motion of carbon nuclei is important, the pictured excursions of the H nuclei are markedly reduced through the normalization process.

Fig. 8, a and *b*, also shows the atomic-contribution patterns, or ACPs, and the group-coupling matrices, or GCMs, defined in [11] and [19], respectively. The ACPs are obtained by splitting the dinuclear terms occurring in *Eqn. 7* between atoms in such a way that the resulting quasi-atomic quantities best reflect the contributions each atom makes to *Raman* and ROA scattering as a result of the combined action of the motion of its nucleus, and the gradients of electronic tensors at its site. The elements of the GCMs, on the other hand, represent groups of atoms (diagonal elements) and the coupling between them (off-diagonal elements). The diagonal elements are obtained by adding, for each group, all mono- and dinuclear intra-group terms, and the off-diagonal elements by adding the dinuclear inter-group terms. In all cases, it is the surface area of the spheres, or circles, which represents the quantity of interest. Dark
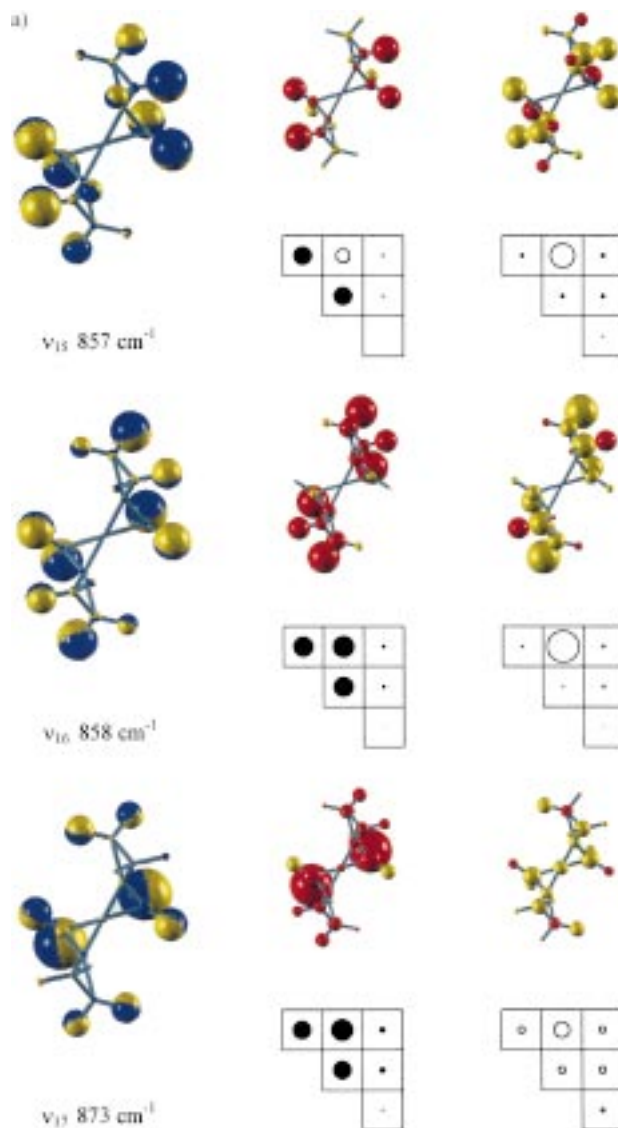
Fig. 8. *Pictorial representation of the vibrational modes a) 15 – 17 and b) 18 – 20 (left), with distributed* Raman *and ROA scattering cross sections*. In the middle and on the right are shown the *Raman* and the ROA atomic contribution patterns (ACPs), respectively, together with the group coupling matrices (GCMs). Group 1 and 2 correspond to the two halves of the molecule, minus the central spiro-C-atom C(5), which in turn represents group 3. Scale factors are arbitrary but identical for all drawings, including those in *Figs. 6 and 9*.

colors (red or black) have been chosen for positive contributions, and light colors (yellow or white) for negative ones.

The quantities represented, for reasons discussed earlier, are the integral scattering cross sections given by *Eqns. 6a* and *6b*. From *Table 2*, it can be seen that qualitative
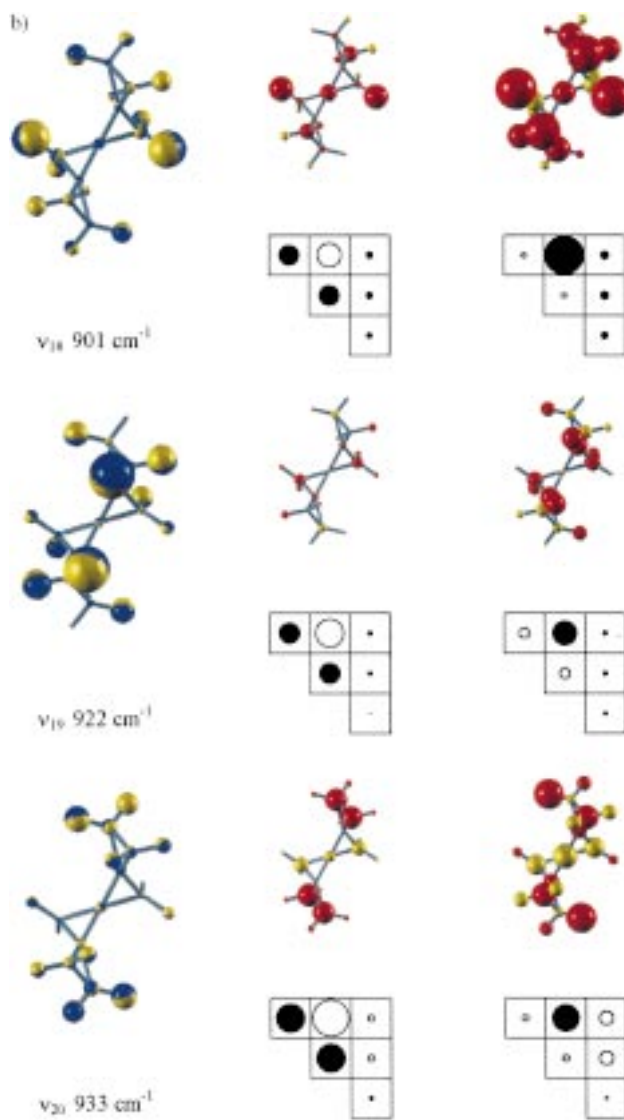
Fig. 8. (cont).

comparison with the backscattering spectra is possible for all vibrations discussed. The modes 15, 17, 19, and 20 of species B are depolarized, and $a^2 = aG' = 0$. For the two slightly polarized modes 16 and 18 of species A, aG' remains negligible, and the value of $90a^2 + 14\beta^2$ in *Eqn. 4a* is largely determined by β^2, as is that of the relevant invariant combination $180a^2 + 40\beta^2$ in *Eqn. 6a*. Quadrupole contributions in backscattering make a more substantial difference, but they are all of the same sign as the magnetic dipole contributions. Moreover, β_A^2 appears with one third of the weight of only β_G^2 in the

Table 2. *Calculated Molecular* Raman *and ROA Invariants for the Vibrational Modes 15 to 20*. Computational details as for *Fig. 4*.

Mode	Ka^2	$K\beta^2$	$\dfrac{K}{c}aG'$	$\dfrac{K}{c}\beta_G^2$	$\dfrac{K}{c}\beta_A^2$
	[10^{-17} Å²/sr]	[10^{-17} Å²/sr]	[10^{-20} Å²/sr]	[10^{-20} Å²/sr]	[10^{-20} Å²/sr]
15	0.000	29.32	0.000	-12.63	-16.22
16	0.196	72.05	0.030	-21.56	-10.88
17	0.000	69.51	0.000	-9.31	-8.23
18	0.282	21.77	0.049	37.83	23.68
19	0.000	5.27	0.000	9.94	3.55
20	0.000	17.68	0.000	6.65	2.71

Table 3. *Integral Circular-Sum and Circular-Difference SCP Scattering Cross Sections, with a Breakdown into Separate Contributions Made by C- and H-Atoms*. Computational details as for *Fig. 4*.

Mode	$^n\sigma_C$ [10^{-14} Å²]	$^n\sigma_H$ [10^{-14} Å²]	$^n\sigma_{SCP}$ [10^{-14} Å²]	$-\Delta^n\sigma_C$ [10^{-17} Å²]	$-\Delta^n\sigma_H$ [10^{-17} Å²]	$-\Delta^n\sigma_{SCP}$ [10^{-17} Å²]	$10^3\Delta$
15	0.85	4.06	4.91	-2.69	-1.54	-4.23	-0.86
16	2.65	9.57	12.22	-3.59	-3.59	-7.18	-0.59
17	4.32	7.33	11.65	-2.24	-0.88	-3.12	-0.27
18	1.95	1.91	3.86	6.27	6.48	12.75	3.30
19	0.39	0.49	0.88	1.08	2.25	3.33	3.77
20	2.67	0.29	2.96	0.05	2.18	2.23	0.75

backscattering formula (*Eqn. 4b*). Even for vibration 15, where the size of β_A^2 is largest compared to β_G^2, quadrupole contributions thus make up less than one-third of observed ROA. This picture is confirmed by the comparison of the Δ values for integral scattering, listed in *Table 3*, with those given for backscattering in *Table 1*. For all six vibrations, one finds that the ratio $\Delta(\pi)/\Delta$ remains in the vicinity of 2.

A question of basic interest that one might ask, with the detailed data of *Fig. 8,a* and *b*, at hand, is to what extent is the large nuclear excursion synonymous with large *Raman* and ROA generation by the pertinent atom. Clearly, only atoms the nuclei of which move can produce *Raman* and ROA intensity, but it is not necessarily the atoms the nuclei of which move the most, which also make the largest contribution to them. This is clearly borne out by the *Raman* ACPs of mode 19 and 20, where the pattern of *Raman* generation bears no resemblance to the pattern of nuclear motion. In mode 20, in particular, the relatively modest C(1), C(2), and C(8), C(9) stretching motions produce the whole of the *Raman* intensity of the molecule, with the motion of C(3), C(5), and C(7) actually subtracting from it. In contrast, in the two modes 17 and 18, there is resemblance between nuclear motion and *Raman* generation.

The picture is equally mixed when *Raman* and ROA generation are compared. Some resemblance can be found in mode 16 and, perhaps, 15, but little or nothing in other modes. This finding is not astonishing. The gradients of true and pseudo-tensors, which enter the expressions for *Raman* and ROA scattering cross sections, respectively, have little in common with each other, neither with respect to direction nor size. There is, therefore, no reason why the patterns of the distribution of σ and $-\Delta\sigma$ over the shape of the molecule should resemble each other.

ACPs and GCMs transform according to the representation of species A of the point group C_2 of the molecule. They do therefore not change sign upon rotation about the C_2 axes, even though the underlying normal mode might do so. If two normal modes are identical, except for one of them transforming according to the A representation and the other according to the B representation, then this will show up in identical group-coupling matrices, except for a sign reversal of all coupling terms between the two C_2-symmetry-related parts of the molecule. Such behavior is readily observed for pairs of vibrations such as 13, 14, or 34, 35. For the 6 vibrations discussed in detail here there is however, no good example of this kind of matched A/B pair, a statement which remained true if the two vibrations 21 and 22 of species A were included in the set. The two vibrations 15 and 16 come closest to it. The relative directions of the calculated nuclear motions on the two halfs of the molecule are opposite in the two modes but their size varies, too, and only the coupling elements in the *Raman* GCMs, but not the ROA GCMs, show opposite signs.

A vexing question that one is invariably tempted to ask when looking at drawings such as those shown in *Fig. 8,a* and *b*, is whether it can somehow be 'seen' from the shape of the normal modes that they lead to large *Raman* or ROA scattering. For small molecules there are reliable, often symmetry-based rules for the *Raman* intensity to be expected. The fact that the symmetric stretching vibration of CO_2, *e.g.*, generates a lot of it and the antisymmetric one none can easily be understood. In polyatomic chiral molecules such insights are less obvious. The record-breaking performance in ROA generation by mode 18, combined with only modest *Raman* generation, can certainly not be glanced from its picture in *Fig. 8,b*. It must be rationalized with the help of computed data.

The ROA ACP of mode 18 shows that the largest contributions are made, in this sequence, by the H-atoms at C(4) and C(6), which move the most by the two C-atoms C(2) and C(9), and by the C-atoms C(1) and C(8). ACPs do not provide direct information on the coupling of nuclear motion that produces them. It would appear unlikely, however, that a ROA of the observed size should be generated within the achiral halves of the molecule, even though nuclear motion in mode 18 is by no means achiral on these fragments. The ROA coupling matrix in *Fig. 8,b*, corroborates this view. Almost all of the ROA produced in vibration 18 is due to coupling terms between the two molecular halves, and not to the chiral nature of the vibrational motion on the fragments themselves. The situation is similar for the other five of the set of six vibrations we discuss here in detail. In all cases, ROA is dominated by coupling between the two halves of the molecule.

The understanding of ROA generation can be improved by reducing the size of the molecular fragments in the coupling matrices. By separating C- and H-atoms, as done in the GCMs of *Fig. 9*, it becomes apparent that most of the positive ROA produced by mode 18 actually results from the interaction of H-atom motion on one molecular half, with the C-atom motion on the other. It is also seen that the ROA generated within the fragments, with the exception of the one representing the central spiro-C-atom, is opposite in sign to that resulting from the interaction between the groups. Such extensive canceling is a common aspect in ROA generation.

Canceling can also be encountered in the generation of *Raman* intensity. Where it occurs it is, however, in general, the *Raman* scattering produced within the groups,
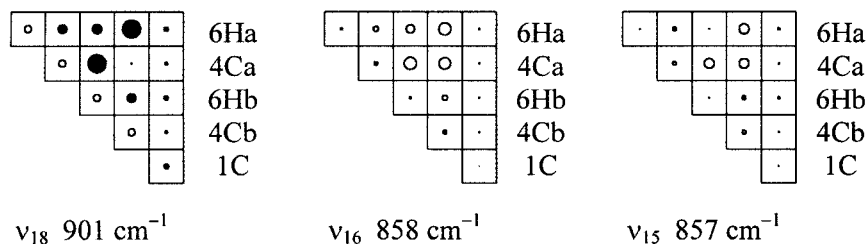
Fig. 9. *ROA Group-coupling matrices for vibrations 15, 16, and 18 with a separation of H-atom and C-atom contributions*. Group 1 and 3: H-atoms of the two halves *a* and *b* of the molecule. Group 2 and 4: C-atoms of the two halves, minus C-atom C(5). Group 5: central spiro-C-atom. In view of the difference in overall size of the matrices shown in *Figs. 8* and *9*, the size of the circles must be judged relative to the size allocated to the individual squares representing matrix elements.

which dominates, with inter-group coupling terms detracting from it. The *Raman* coupling matrices of vibration 15, 18, 19, and 20 in *Fig. 8* exemplify this. The difference in ROA generation can readily be understood. Polarizability-theory expressions for *Raman* intensities are semi-definite quadratic forms [19]. Mononuclear terms are, therefore, positive and dominate the sum of terms, in contrast to the situation in ROA.

In mode 18, on balance, C-atoms and H-atoms make about equal contributions to net ROA generation, as can be seen from *Table 3*. This indicates, in view of the weighting scheme that we use in attributing dinuclear terms to atoms [11], that the smaller excursions of the C-atoms are compensated by larger and/or more favorably oriented tensor gradients on them. The same holds for *Raman* generation in mode 18. ROA Generation in the strongly negative mode 16 is again balanced between C- and H-atoms, and it also shows, as seen from *Fig. 9*, a similar, though sign-reversed, pattern to mode 18 for the coupling terms between them. *Raman* generation, on the other hand, is differently distributed and mostly carried by the H-atoms. The picture with respect to the C- and H-atom contributions to ROA and *Raman* scattering stays mixed throughout the remainder of spectral region 2, as evidenced by the additional vibrations collected in *Table 3*.

An aspect in which the two vibrations with the largest negative and largest positive ROA of the discussed set are strikingly different is their overall shape, even though both of them are of species A. The dominant component of nuclear motion in the negative vibration 16 is along the axis of the helix formed by the molecule, thereby conveying the impression of an extension of the molecule in length. In contrast, nuclear motion in the positive vibration 18 has a strong component perpendicular to this axis, which gives the impression of a distortion in width. The *Raman* and ROA atomic contribution patterns nicely confirm this view. It is hoped that such global aspects will turn out, with time, to be helpful for a qualitative understanding of observed *Raman* and ROA scattering of inherently chiral chromophores, for which traditional methods of vibrational analysis, such as the standard percentage decomposition of vibrations into wagging, twisting, and rocking motion, appear to represent a hopelessly inadequate tool for large spectral regions.

REFERENCES

[1] L. D. Barron, M. P. Bogaard, A. D. Buckingham, *Nature* **1973**, *241*, 113.

[2] G. Holzwarth, E. C. Hsu, H. S. Mosher, T. R. Faulkner, A. Moscowitz, *J. Am. Chem. Soc.* **1974**, *96*, 251.

[3] L. D. Barron, A. D. Buckingham, *J. Chem. Soc., Chem. Commun.* **1973**, 152.

[4] L. A. Nafie, J. C. Cheng, P. J. Stephens, J. Am. Chem. Soc. **1975**, *97*, 3842; L. A. Nafie, T. A. Keiderling, P. J. Stephens, *J. Am. Chem. Soc.* **1976**, *98*, 2715.

[5] W. Hug, S. Kint, G. F. Bailey, J. R. Scherer, *J. Am. Chem. Soc.* **1975**, *97*, 5589.

[6] D. Che, L. A. Nafie, *Appl. Spectrosc.* **1993**, *47*, 544.

[7] W. Hug, 'Raman Optical Activity, Spectrometers' in 'Encyclopedia of Spectroscopy and Spectrometry', Eds. J. Lindon, G. Tranter, and J. Holmes, Academic Press, London, 1999, pp. 1966 – 1976.

[8] M. A. Lowe, P. J. Stephens, G. A. Segal, *Chem. Phys. Lett.* **1986**, *123*, 108.

[9] P. L. Polavarapu, *J. Phys. Chem.* **1990**, *94*, 8106.

[10] P. J. Stephens, F. J. Devlin, C. S. Ashvar, C. F. Chabalowski, M. J. Frisch, *Faraday Discuss.* **1994**, *99*, 103.

[11] W. Hug, 'Raman Optical Activity Spectroscopy' in 'Handbook of Vibrational Spectroscopy, Volume 1: Theory and Instrumentation', Eds. J. M. Chalmers and P. R. Griffiths, John Wiley and Sons, Chichester, 2001, in press.

[12] L. Fitjer, J.-M. Conia, *Angew. Chem.* **1973**, *85*, 832; *Angew. Chem., Int. Ed.* **1973**, *12*, 761.

[13] A. de Meijere, A. F. Khlebnikov, R. R. Kostikov, S. I. Kozhushkov, P. R. Schreiner, A. Wittkopp, D. S. Yufit, *Angew. Chemie* **1999**, *111*, 3682.

[14] W. Hug, G. Hangartner, *J. Raman Spectrosc.* **1999**, *30*, 841.

[15] W. Hug, in preparation.

[16] L. Hecht, L. A. Nafie, *Mol. Phys.* **1991**, *72*, 441.

[17] W. Hug, H. Surbeck, *Chem. Phys. Lett.* **1979**, *60*, 186.

[18] G. Placzek, 'Rayleigh-Streuung und Raman-Effekt' in ' Handbuch der Radiologie, Vol. VI', Ed. E. Marx, Akademische Verlagsgesellschaft, Leipzig, 1934, pp. 205 – 374.

[19] W. Hug, *Chem. Phys.*, in press.

[20] *GAUSSIAN98*, *Gaussian Inc.*, Pittsburgh, PA.

[21] T. Helgaker, H. J. Aa. Jensen, P. Joergensen, J. Olsen, K. Ruud, H. Aagren, T. Andersen, K. L. Bak, V. Bakken, O. Christiansen, P. Dahle, E. K. Dalskov, T. Enevolsen, B. Fernandez, H. Heiberg, H. Hettema, D. Jonsson, S. Kirpekar, R. Kobayashi, H. Koch, K. V. Mikkelsen, P. Norman, M. J. Packer, T. Saue, P. R. Taylor, O. Vahtras, 'DALTON release 1.0 (1997), an electronic structure program'.

[22] G. Zuber, G. Hangartner, W. Hug, *Chem. Phys. Lett.*, in preparation.

[23] W. Hug *et al.*, *Helv. Chim. Acta*, in preparation.